Chemical Science

ROYAL SOCIETY OF CHEMISTRY | Celebrating IYPT 2019

EDGE ARTICLE
Lijun Yang, Xizhang Wang, Zheng Hu *et al.*
Stabilizing the active phase of iron-based Fischer–Tropsch catalysts for lower olefins: mechanism and strategy

EDGE ARTICLE

Stabilizing the active phase of iron-based Fischer–Tropsch catalysts for lower olefins: mechanism and strategy†

Ou Zhuo,[a] Lijun Yang, (ID) *[a] Fujie Gao,[a] Bolian Xu,[a] Qiang Wu, (ID) [a] Yining Fan,[a] Yu Zhang,[b] Yufei Jiang,[a] Runsheng Huang,[b] Xizhang Wang (ID) *[a] and Zheng Hu (ID) *[a]

Fischer–Tropsch synthesis of lower olefins (FTO) is a classical yet modern topic of great significance in which the supported Fe-based nanoparticles are the most promising catalysts. The performance deterioration of catalysts is a big challenge due to the instability of the nanosized active phase of iron carbides. Herein, by *in situ* mass spectrometry, theoretical analysis, and atmospheric- and high-pressure experimental examinations, we revealed the Ostwald-ripening-like growth mechanism of the active phase of iron carbides in FTO, which involves the cyclic formation–decomposition of iron carbonyl intermediates to transport iron species from small particles to large ones. Accordingly, by suppressing the formation of iron carbonyl species with a high-N-content carbon support, the size and structure of the active phase were regulated and stabilized, and durable iron-based catalysts were conveniently obtained with the highest selectivity for lower olefins up to 54.1%. This study provides a practical strategy for exploring advanced FTO catalysts.

Introduction

Lower olefins ($C_2^=–C_4^=$), the key building blocks in modern chemical industry, are produced mainly by cracking hydrocarbons from petroleum reserves.[1] Recently, Fischer–Tropsch synthesis of lower olefins (FTO) has become a hot topic since this route uses sustainable syngas (CO and H_2) as the feedstock, independent of the limited petroleum.[1–7] The key for large-scale application of FTO is to develop catalysts with high $C_2^=–C_4^=$ selectivity, low methane production, and meanwhile long lifetimes. To date, numerous efforts have been devoted to enhancing the $C_2^=–C_4^=$ selectivity *via* regulating the catalytic active species,[4–8] catalyst supports,[9–13] and promoters.[14–17] The supported Fe nanoparticles are particularly attractive owing to their high catalytic activity and selectivity for $C_2^=–C_4^=$, as well as the low cost.[4,9–15,18–20] Usually, the Fe-based active phase should remain in the size range of several nanometers due to the high selectivity of $C_2^=–C_4^=$, since FTO reactions are sensitive to the catalyst structure.[18] However, Fe nanoparticles undergo multiple changes during FTO, including reduction, carbonization and long-term reaction with syngas, which makes the active-phase particles easily grow into larger-sized low-activity

ones, leading to severe performance degradation.[13,14,18–21] Therefore, the fine regulation of the size and structure of the active phase is essential to achieve high activity, selectivity, and durability of the catalyst. Though some progress has been made by physically encapsulating or confining the active-phase nanoparticles inside porous supports,[12,13,22] a fundamental understanding of the active-phase growth under real reaction conditions is still missing, which is the basis for designing durable FTO catalysts with high performance.

In our recent study, by making use of the anchoring effect[23,24] and the intrinsic basicity of nitrogen-doped carbon nanotubes (NCNT), iron nanoparticles were conveniently dispersed, and the so-constructed Fe/NCNT catalysts presented superb catalytic performance in FTO and much improved stability.[10] The correlation between the catalyst stability and N-doped carbon supports inspires us to get insight into the underlying mechanism. Our recently developed 3D hierarchical nitrogen-doped carbon nanocages (hNCNC) provide us a good platform to implement this study, which feature a tunable nitrogen content in a wide range in addition to a high specific surface area (S_{BET}) and coexisting micro–meso–macropores.[25–27] Herein, by *in situ* mass spectrometry, theoretical analysis, and atmospheric- and high-pressure experimental examinations, the iron carbonyl-mediated growth mechanism of the active phase of iron carbide (Fe_xC_y) nanoparticles is revealed for the first time, which follows an Ostwald-ripening-like growth process. This mechanism is applied for optimizing durable catalysts by suppressing the formation of iron carbonyl intermediates with a high-N-content (12.0 at%) hNCNC support and optimized reaction conditions.

[a]Key Laboratory of Mesoscopic Chemistry of MOE, School of Chemistry and Chemical Engineering, Nanjing University, Nanjing 210023, China. E-mail: lijunyang@nju.edu.cn; wangxzh@nju.edu.cn; zhenghu@nju.edu.cn

[b]School of Physics, Nanjing University, Nanjing 210093, China

† Electronic supplementary information (ESI) available. See DOI: 10.1039/c9sc01210a

The optimal catalyst presents a high $C_2^=$–$C_4^=$ selectivity (up to 54.1%) and exceptional stability, and the Fe_xC_y nanoparticles only show a slight increase in size even after reaction for 200 h. This study opens a new avenue for exploring advanced durable FTO catalysts.

Results and discussion

Catalyst preparation and characterization

Three hNCNC supports were prepared similar to our previous reports,[25–27] with N contents of 3.0, 8.1 and 12.0 at%, denoted as hNCNC-1, hNCNC-2 and hNCNC-3, respectively. A pristine hierarchical carbon nanocage (hCNC) support was also prepared for comparison. All supports present a 3D hierarchical architecture constructed by interconnected hollow nanocages of 10–30 nm in size and 3–7 graphitic layers in shell thickness. This unique mesostructure leads to the coexistence of abundant micro-, meso-, and macropores and ultrahigh S_{BET} (>1800 m^2 g^{-1}). Catalysts with tunable Fe loadings of ca. 10–40 wt% were conveniently prepared by wet impregnation without any pre-treatment to the supports,[10] denoted as nFe/hNCNC or nFe/hCNC (n represents the nominal Fe loading in weight percentage). The experimentally measured Fe loadings are very close to the nominal ones (see the Experimental section; Experimental procedures, Fig. S1, Tables S1 and S2 in the ESI†).

For all the fresh catalysts, Fe-based nanoparticles are well dispersed on the supports with narrow size distributions mainly as Fe_3O_4 nanoparticles (Fig. S2–S4†). At an Fe loading of ca. 10 wt%, the average size of Fe_3O_4 nanoparticles decreases monotonously from 7.4 to 4.3 nm with increasing the N content from 0 to 12.0 at%, accompanied by the narrowing of size distribution (Fig. S3†). At a fixed N content of 12.0 at%, the average size of Fe_3O_4 nanoparticles increases from 4.3 to 7.0 nm with increasing the Fe loading from 9.5 to 41.5 wt% (Fig. S4†). The excellent dispersion is attributed to the large S_{BET} and especially the nitrogen anchoring or coordination effects as revealed in our previous studies.[10,23,24]

Mechanism and strategy

In general, there are two typical particle growth processes: (i) particle migration and coalescence; (ii) Ostwald ripening, i.e., the growth of large particles at the expense of smaller particles through the migration of single atoms or small clusters.[28,29] Particle migration and coalescence are commonly observed for the supported catalysts, when the reaction temperature is higher than the Tammann temperature (T_{ta}) of the active phase, about half of the bulk melting point ($T_{melting}$).[28] This type of particle growth process could be alleviated/suppressed by encapsulating/confining the nanoparticles inside porous supports.[29] For iron carbides, since $T_{melting} \geq 1153 \,^\circ C$ (1426 K),[30] the corresponding T_{ta} is ca. 440 $^\circ C$ (713 K), i.e., higher than the reaction temperature of FTO ($\leq 350 \,^\circ C$), which suggests the minor contribution of particle migration and coalescence to the active-phase growth of Fe-based FTO catalysts. Thus, Ostwald ripening, which usually accounts for the particle growth in solid solution and colloidal solution,[31] might be dominant in FTO

reactions. Actually, in a recent study on cobalt-based Fischer–Tropsch catalysts, the Ostwald ripening mechanism was speculated despite the lack of direct experimental evidence.[32,33]

To have an intuitive impression on the growth of the active phase of Fe_xC_y nanoparticles in FTO, we performed a control experiment as follows. A fresh 10Fe/hNCNC-3 catalyst was firstly activated under FTO conditions for 5 h, and then CO was switched off. After an additional 55 h treatment in H$_2$ at 350 $^\circ C$, the morphology and particle size distribution were barely changed for the Fe_xC_y nanoparticles, much different from the case for the spent 10Fe/hNCNC-3 catalyst after FTO reaction for 60 h, i.e., in the presence of CO (Fig. S5†). This result indicates that CO plays a vital role for the growth of Fe_xC_y nanoparticles, while the particle migration and coalescence have a minor contribution.

As known, under suitable conditions, CO can react with Fe species to produce gaseous iron carbonyls,[34] and iron carbonyls can also decompose into Fe_xC_y.[35,36] Thus, we speculated that the gaseous iron carbonyls might be responsible for the growth of Fe_xC_y nanoparticles via in situ formation, diffusion and decomposition. According to thermodynamic analysis, the formation of iron carbonyls from iron carbides (s) and CO (g) is a strongly exothermal and volume-reducing reaction. Taking the formation of iron pentacarbonyl as an example, the equilibrium partial pressure of gaseous iron pentacarbonyl ($p_{Fe(CO)_5}$) decreases sharply on increasing the reaction temperature (T) or decreasing the partial pressure of CO (p_{CO}) based on the van't Hoff equation and Le Châtelier's principle (See Fig. S6† for detailed analysis).[37] To verify this speculation, in situ mass spectrometry (MS) was employed to detect iron carbonyls as shown in Fig. 1. The signals of m/z (mass to charge ratio) in the range of 40–200 are well assigned to iron carbonyls and their fragments, clearly indicating the formation of iron carbonyls in CO flow (Fig. 1b).[38] Moreover, the intensity of the $m/z = 56$ signal, which is characteristic of iron carbonyls, decreases with increasing T in the high temperature range (e.g., $T > \sim 180 \,^\circ C$ at a p_{CO} of 1.0 MPa), and decreases significantly when reducing p_{CO} from 1.0 to 0.1 MPa for all the four samples, in good agreement with our theoretical predictions (Fig. 1c and S6†). In the low temperature range (e.g., $T < \sim 180 \,^\circ C$ at a p_{CO} of 1.0 MPa), the increasing signal with T is associated with the rapidly increasing formation of iron carbonyls in the kinetically controlled range. Thus, a volcano shape profile appears for the signal of $m/z = 56$ versus T (Fig. 1c). It is notable that the signal of $m/z = 56$ presents a decreasing tendency with increasing the N content of the supports either for $p_{CO} = 1.0$ MPa or for $p_{CO} = 0.10$ MPa (Fig. 1c). This result indicates that the formation of iron carbonyls can be effectively suppressed by using N-doped carbon supports, which is supported by a density functional theory (DFT) study on the formation of $Fe(CO)_5$ by chemisorption of CO on a single Fe atom supported on a pristine or N-doped graphitic plane (Fig. 1d and S7†). The results demonstrate that pyridinic-N possesses the best capability for the suppression, on which the conversion from $Fe(CO)_3$ to $Fe(CO)_4$ (S-4 → S-5 in Fig. 1d) is endothermic due to the strong binding between Fe and pyridinic-N (Fig. S8†). The calculations of the projected d-band centers (E_d) reveal that the E_d of the supported
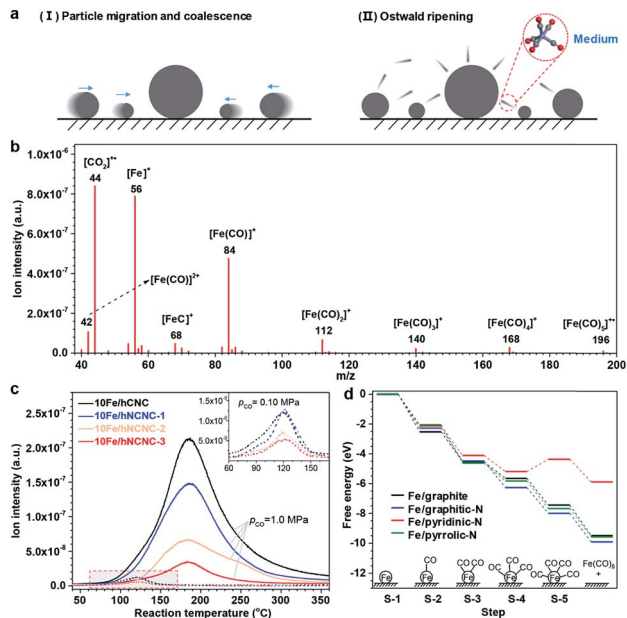
Fig. 1 *In situ* mass spectroscopic examination of iron carbonyls and DFT simulation of its formation *via* the carbonylation of iron species. (a) Two typical particle growth mechanisms. (b) Signals of *m/z* using the bar scanning model for 10Fe/hCNC. Reaction conditions: 175 °C, 1.0 MPa CO flow of 10 mL min^{-1}. (c) Signals of *m/z* = 56 using the trend scanning model. Catalysts: 10Fe/hCNC, 10Fe/hNCNC-1, 10Fe/hNCNC-2 and 10Fe/hNCNC-3. Reaction conditions: 0.10 and 1.0 MPa CO flow of 10 mL min^{-1}. The inset shows an enlarged view of the dashed curves for p_{CO} = 0.10 MPa in the marked region. (d) The free energy diagram for the formation of Fe(CO)$_5$ on a single Fe atom at the pristine or N-doped graphitic plane. The supported Fe single atom without CO adsorption is selected as the referenced zero point. The optimized configurations are presented in Fig. S7.†

Fe atom downshifts by 0.45 eV for the pyridinic N-doped graphitic plane with respect to the pristine one (Fig. S9†). According to the d-band model, the downshifted E_d weakens the binding between Fe and CO,[39] leading to the suppression of iron carbonyl formation on the pyridinic-N doped carbon supports. In addition, the detachment of the iron carbonyl species from the N-doped carbon support is more difficult than that from the pristine carbon support due to the N anchoring effect, which could hinder the transportation of iron carbonyl species and thus favor the suppression of particle growth (Fig. S7†). Further DFT studies on the carbonylation process for the Fe$_5$C$_2$ cluster also indicate the suppression capability of pyridinic-N for the formation and detachment of iron carbonyl species (Fig. S10 and S11†). The pyridinic-N in hNCNC, about 24–32% of the total nitrogen content (Table S1†), makes the formation and transportation of gaseous iron carbonyls difficult.

Based on the above results, the correlation between the gaseous iron carbonyls and the growth of Fe$_x$C$_y$ nanoparticles could be established. According to Fig. 1c, the lower T or the higher p_{CO} is beneficial to the formation of more iron carbonyls, *i.e.* the increase of the partial pressure of iron carbonyl intermediates ($p_{Fe(CO)_x}$). Hence, we examined the dependence of the final average sizes of Fe$_x$C$_y$ nanoparticles on

the amount of iron carbonyls by changing T and p_{CO} for the optimized catalyst of 35Fe/hNCNC-3 after 60 h on stream in FTO. With decreasing T from 350 to 300 and 250 °C at a fixed p_{CO} of 0.05 MPa, the average size increases from 7.0 to 8.3 and 8.5 nm, respectively (Fig. S12†). It is worth mentioning that this result contradicts the particle migration and coalescence situation, *i.e.*, the higher T usually leads to more serious particle growth,[28,29] but is in agreement with our expectation based on the exponential increase of $p_{Fe(CO)_x}$ with decreasing T (Fig. 1c). Moreover, with increasing p_{CO} from 0.05 to 1.0 MPa at a fixed temperature of 350 °C, the average size evidently increases from 7.0 to 11.8 nm, again in agreement with our expectation according to the much increased $p_{Fe(CO)_x}$ (Fig. 1c and S12†). The results of the designed experiments confirm that the *in situ*-formed gaseous iron carbonyls are responsible for the growth of Fe$_x$C$_y$ nanoparticles. This is the first experimental confirmation of the iron carbonyl-mediated growth mechanism of the active phase in Fischer–Tropsch synthesis. This finding can be applied to guide the catalyst design as demonstrated below.

Catalytic performance

According to the iron carbonyl-mediated particle growth mechanism, the growth of Fe$_x$C$_y$ nanoparticles could be alleviated by suppressing the generation of iron carbonyls. In addition to selecting suitable reaction conditions such as T and p_{CO}, using the N-doped carbon support and/or increasing the initial particle size to lower the surface energy could also decrease the $p_{Fe(CO)_x}$. So we systematically examined the influences of N content and Fe-loading on the particles' growth and FTO catalytic performance, as shown in Fig. 2 and Table 1.

After *ca.* 10 h incubation, the catalysts with a low-Fe-loading (*ca.* 10 wt%) reach relatively steady selectivities. With increasing N content of 0–12.0 at%, the C$_2^=$–C$_4^=$ selectivity at a time on stream (TOS) of 60 h increases from 44.4 to 52.1%, while those for methane and lower alkanes (C0 2–C0 4) are suppressed at a low level for promoter-free catalysts (Table 1; Fig. S13†).[18,19,40] Meanwhile, the average sizes of the Fe$_x$C$_y$ nanoparticles in the spent catalysts decreased from 17.9 to 8.4 nm (Fig. 2a′–d′), which demonstrates a powerful regulation of the active phase by the nitrogen content of the support. In contrast, for the fixed high-N-content hNCNC-3 support (12.0 at%), with increasing Fe loading of 9.5–41.5 wt%, the C$_2^=$–C$_4^=$ selectivity remains at a high level above 50.8% and reaches a maximum of 54.1% for 35Fe/hNCNC-3 (Table 1). Such a high selectivity is mainly attributed to the intrinsic basicity of hNCNC-3 due to the high N content.[10] Despite the wide-range change of Fe loading (9.5–41.5 wt%), the average sizes of the Fe$_x$C$_y$ nanoparticles in the spent catalysts only slightly changed within 6.2–8.4 nm (Fig. 2d–h, d′–h′), which demonstrates the confinement capability of the high N content to the active phase. Actually, all the catalysts supported on the high-N-content hNCNC-3 present a high sintering resistance in comparison with their counterparts based on the lower-N-content hNCNC and undoped hCNC supports (Fig. 2, S3 and S4†). These results indicate that N-doping into the carbon support is an effective strategy to regulate and stabilize
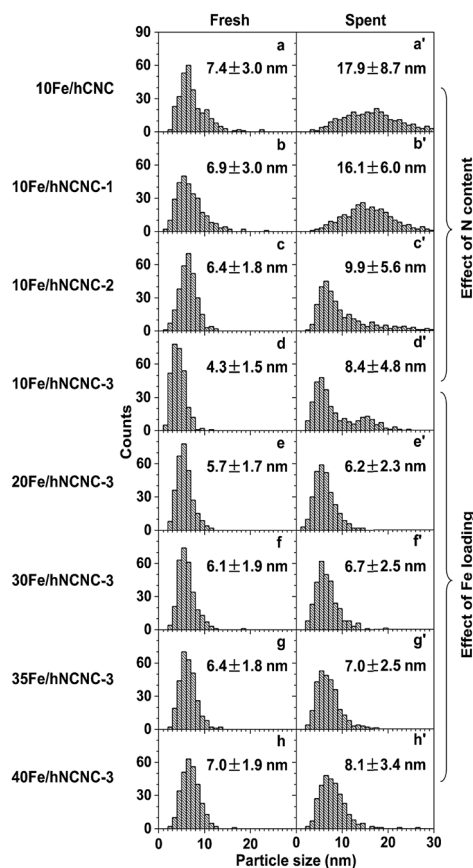
Fig. 2 Influence of N content and Fe loading on the iron carbonyl-mediated particle growth. (a–d and a'–d') Particle size histograms of fresh (a–d) and corresponding spent (a'–d') catalysts with an Fe loading of ca. 10 wt% on the supports with a nitrogen content of 0, 3.0, 8.1 and 12.0 at%, respectively. (d–h and d'–h') Particle size histograms of fresh (d–h) and corresponding spent (d'–h') catalysts supported on hNCNC-3 with an Fe loading of 9.5, 20.1, 31.4, 36.8 and 41.5 wt%, respectively. Reaction conditions: 350 °C, 0.10 MPa, CO/H$_2$ = 1, TOS = 60 h. Corresponding TEM images of the catalysts are presented in Fig. S3 and S4.†

the Fe-based active phase size for FTO due to the strong suppression effect on the formation of iron carbonyls (Fig. 1c and d). In addition, the results at high pressure (1.0 MPa) also demonstrate the stabilizing effect of the N-doped carbon

support on the Fe-based active phase size to improve the catalytic stability for FTO (Fig. S14 and S15†).

The iron carbonyl-mediated particle growth mechanism can also be applied to well understand the experimental phenomena in this study. We noticed that the core–shell particles, which are not present in the fresh catalysts, are frequently observed in the spent FTO catalysts (Fig. S3, S5 and S12†). Actually, similar core–shell structures were also observed in the literature, and the shell was usually regarded as the carbon layer due to carbon deposition.[14,15] To elucidate the formation of this unique structure, we examined the morphological evolution of the spent 10Fe/hNCNC-3 catalyst after different FTO reaction times of 5, 10 and 60 h, respectively, as presented in Fig. 3. The fresh catalyst is composed of well-dispersed nanoparticles of ca. 4.3 nm in average size (Fig. 3a). In the spent catalyst, core–shell particles appear, and the average size of the cores increases from 6.4 to 7.3 and 7.9 nm with increasing the reaction time from 5 to 10, and 60 h, accompanied by the diminishing of small-sized nanoparticles (Fig. 3b–d and S16†). Typical high-resolution transmission electron microscopy (TEM) images and energy-dispersive X-ray spectroscopy (EDS) line scanning analysis indicate that both the core and the shell are mainly composed of Fe$_x$C$_y$ (Fig. 3e–h and S17†).

Based on the iron carbonyl-mediated mechanism for the growth of Fe$_x$C$_y$ nanoparticles, the formation process of the core–shell structure could be figured out as shown in Fig. 3i. After the initial activation, the Fe$_3$O$_4$ nanoparticles with different sizes in the fresh catalyst were converted to the corresponding Fe$_x$C$_y$ nanoparticles (Step 1). During FTO, a competition of two reversible reactions occurs on the surface of Fe$_x$C$_y$ nanoparticles (Step 2). The forward one is the formation of gaseous iron carbonyl species (Fe(CO)$_x$) via the carbonylation of Fe$_x$C$_y$ (yellow arrows in Fig. 3i). The backward one is the decomposition of the re-adsorbed iron carbonyl species back into Fe$_x$C$_y$ (blue arrows in Fig. 3i). The competition result depends on the sizes of the Fe$_x$C$_y$ nanoparticles. For small-sized nanoparticles, the forward reaction is more favorable due to the high surface energy,[29,41] leading to gradual shrinking and final disappearance. For large-sized nanoparticles, the backward reaction is more favorable since the large size is beneficial to capturing the gaseous iron carbonyl species.[37] When the captured iron carbonyl species are more than that needed for

Table 1 FTO results over different catalysts^a

Sample	N content (at%)	Fe loading (wt%)	CO conversion (%)	CO$_2$ selectivity (%)	Hydrocarbon distribution (at% of C)				O/P^b
					CH$_4$	C$_2^=$–C$_4^=$	C$_2^0$–C$_4^0$	C$_{5+}$	
10Fe/hCNC	0	10	1.7	16.5	27.1	44.4	4.7	23.8	9.4
10Fe/hNCNC-1	3.0	10	2.3	21.2	26.1	46.6	4.1	23.2	11.4
10Fe/hNCNC-2	8.1	10	1.9	22.4	23.8	51.0	4.2	21.0	12.1
10Fe/hNCNC-3	12.0	10	1.5	28.3	25.7	52.1	4.6	17.5	11.3
20Fe/hNCNC-3	12.0	20	2.1	32.1	25.1	53.9	4.1	16.9	13.2
30Fe/hNCNC-3	12.0	30	2.8	34.9	24.9	53.6	3.6	17.8	14.9
35Fe/hNCNC-3	12.0	35	3.5	39.4	**25.0**	**54.1**	3.3	17.6	16.4
40Fe/hNCNC-3	12.0	40	3.2	38.7	24.7	50.8	3.0	21.4	16.9

^{a} Reaction conditions: 350 °C, 0.10 MPa, CO/H$_2$ = 1, TOS = 60 h, gas hourly space velocity (GHSV) = 12 000 mL h^{-1} g^{-1}. ^{b} O/P is the C$_2^=$–C$_4^=$/C$_2^0$–C$_4^0$ ratio. Note: according to the five times repeated measurements, the statistical standard deviation for CO conversions is less than ±0.1%.
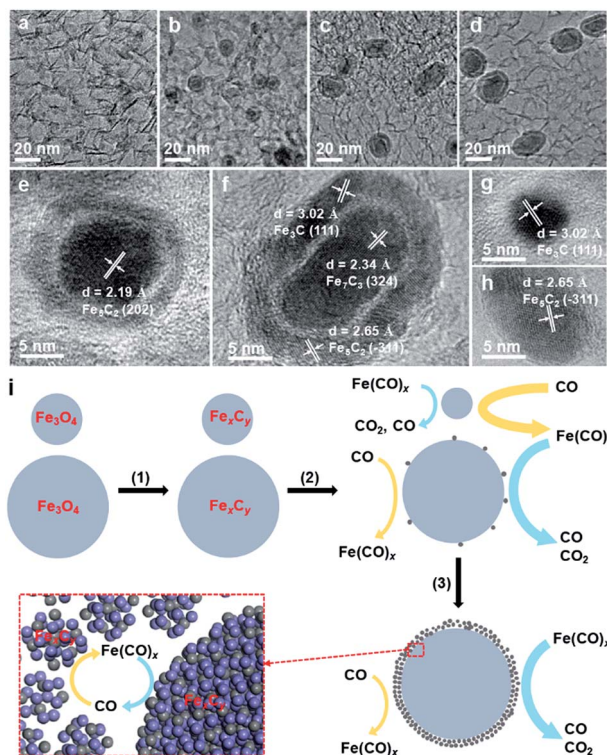
---

outstanding stability (Fig. S18†). We also noted that, with increasing N-doping content, the carbon deposition becomes alleviated for the spent catalysts and even disappears for that with the highest N content (12.0 at%), suggesting the favorable effect of N-doping on the resistance to carbon deposition (Fig. S3, S4 and S19†). High-resolution TEM and Mössbauer characterization indicates the spent catalyst is composed of the crystalline iron carbides such as χ-Fe_5C_2, Fe_7C_3 and θ-Fe_3C, which are the active phase for FTO, and some Fe^{2+} species (Fig. S20†).[19,36,43]

The preceding experimental results and analysis confirm that the iron carbonyl-mediated particle growth dominates the durability of FTO catalysts. The in situ-formed iron carbonyl species mediate the mass transfer from the small particles to the large ones, similar to the case of Ostwald ripening.[28,29] N-doping into a carbon support is an effective strategy to regulate and stabilize the Fe-based active phase size for FTO due to the strong suppression effect on the formation of iron carbonyls. By taking a high-N-content carbon support and optimizing reaction conditions (T and p_{CO}) to stabilize the size and structure of the active phase, durable iron-based catalysts with high $C_2^=$–$C_4^=$ selectivity have been obtained conveniently.

Conclusions

The iron carbonyl-mediated growth mechanism of the active phase of iron carbide (Fe_xC_y) nanoparticles in FTO is revealed for the first time by in situ mass spectrometry, theoretical analysis, and atmospheric- and high-pressure experimental examinations. The in situ-formed iron carbonyl species mediate the mass transfer from small particles to the large ones, similar to the case of Ostwald ripening, which is also responsible for the formation of the observed core–shell structure. The growth and/or the formation of the core–shell structure of Fe_xC_y particles are the main causes of the deterioration of the FTO performance. N-doping into carbon supports can suppress the formation of iron carbonyls, and thus effectively regulates the sizes of Fe_xC_y nanoparticles and alleviates the formation of core–shell structures. Based on this understanding, durable Fe-based catalysts have been conveniently constructed by using the high-N-content hNCNC as the support, and present a high $C_2^=$–$C_4^=$ selectivity with a maximum up to 54.1% under the optimal reaction conditions. Even after FTO reaction for 200 h, the optimized catalyst only shows a slight increase in sizes of Fe_xC_y nanoparticles and retains the high selectivity. The deep insight into the growth mechanism of the Fe-based active phase in this study provides a promising strategy toward advanced FTO catalysts by suppressing the formation of iron carbonyl species with the high-N-content carbon supports and optimized conditions. Such a strategy could also be referential in catalyst design for reactions involving some other metal catalysts and CO reactants.

Experimental section

Catalyst preparation and characterization

The pristine and nitrogen-doped carbon nanocages were synthesized as described in the Experimental procedures in the ESI.† Supported Fe catalysts were prepared by wet impregnation. Briefly, the designated amount of ammonium iron citrate was dissolved in 20 mL distilled water into a Teflon beaker, added with 0.6 g of the support. After impregnation of 24 h, the sample was dried at 100 °C in a hot air oven, and then calcined at 360 °C in an Ar flow for 2 h. When cooling down naturally to ambient temperature, the sample was passivated in 1 vol% O_2-containing argon flow for 0.5 h. The resultant nFe/hNCNC or nFe/hCNC catalyst has a nominal Fe weight loading (n) of 10, 20, 30, 35, and 40%, respectively. TEM and high-resolution TEM images were taken on a JEM-2100F (JEOL) operated at 200 kV. Histogram plots of Fe nanoparticle size distributions were derived from 300 nanoparticles.

In situ detection of iron carbonyls

Iron carbonyls were detected using an in situ mass spectrometer (AMETEK, DYCOR DME300MS) through capillary sampling. Typically, 200 mg of the catalyst was reduced at 350 °C by H_2 flow (20 mL min^{-1}) for 2 h. After cooling to room temperature, pure CO at 0.10 or 1.0 MPa pressure was fed into the reactor at a flow rate of 10 mL min^{-1}. The MS signals of m/z = 40–200 were sampled using the scanning bar model at a reaction temperature of 175 °C, to confirm the formation of iron carbonyls. The in situ MS signals of m/z = 56 were recorded using the scanning trend model from 30 to 360 °C at a heating rate of 4.0 °C min^{-1}, to examine the temperature-dependence for the formation of iron carbonyl.

Catalytic testing

FTO reactions were performed at 0.10 (or 1.0) MPa and 350 °C using a fixed-bed micro-reactor. Typically, 50 mg of the catalyst was diluted with 3.0 g of quartz sand (20–40 mesh) to achieve isothermal plug-flow conditions, which was then charged into a passivated stainless steel tube reactor. The catalyst was reduced at 350 °C by H_2 flow (20 mL min^{-1}) for 2 h. Then, the gas mixture of H_2/CO/Ar (47.5/47.5/5.0) was fed into the reactor at a certain flow rate with Ar as an internal standard. All the hydrocarbons were on-line analyzed using a gas chromatograph (Qiyang GC9860) equipped with two capillary columns. C_1–C_4 hydrocarbons were analyzed using a PLOT-Al_2O_3 capillary column and C_5–C_{30} hydrocarbons were analyzed using a HP-PONA capillary column, respectively. CO, CO_2, and CH_4 were analyzed using another GC9860 with a thermal conductivity detector with a TDX-01 column. The hydrocarbon selectivities were calculated on a carbon basis, with the exception of CO_2.

DFT calculations

Periodic DFT calculations were carried out with the DMol^3 Package embedded in Materials Studio 8.0. Details are presented in the Experimental procedures in the ESI.†

Conflicts of interest

There are no conflicts to declare.

Acknowledgements

Notes and references

1 H. M. Torres Galvis and K. P. de Jong, *ACS Catal.*, 2013, **3**, 2130–2149.

2 K. Cheng, J. C. Kang, D. L. King, V. Subramanian, C. Zhou, Q. H. Zhang and Y. Wang, *Adv. Catal.*, 2016, **60**, 125–208.

3 W. Gao, R. Gao, Y. F. Zhao, M. Peng, C. Q. Song, M. Z. Li, S. W. Li, J. J. Liu, W. Z. Li, Y. C. Deng, M. T. Zhang, J. L. Xie, G. Hu, Z. S. Zhang, R. Long, X. D. Wen and D. Ma, *Chem*, 2018, **4**, 2917–2918.

4 H. M. Torres Galvis, J. H. Bitter, C. B. Khare, M. Ruitenbeek, A. I. Dugulan and K. P. de Jong, *Science*, 2012, **335**, 835–838.

5 L. S. Zhong, F. Yu, Y. L. An, Y. H. Zhao, Y. H. Sun, Z. J. Li, T. J. Lin, Y. J. Lin, X. Z. Qi, Y. Y. Dai, L. Gu, J. S. Hu, S. F. Jin, Q. Shen and H. Wang, *Nature*, 2016, **538**, 84–87.

6 F. Jiao, J. J. Li, X. L. Pan, J. P. Xiao, H. B. Li, H. Ma, M. M. Wei, Y. Pan, Z. Y. Zhou, M. R. Li, S. Miao, J. Li, Y. F. Zhu, D. Xiao, T. He, J. H. Yang, F. Qi, Q. Fu and X. H. Bao, *Science*, 2016, **351**, 1065–1068.

7 K. Cheng, B. Gu, X. L. Liu, J. C. Kang, Q. H. Zhang and Y. Wang, *Angew. Chem., Int. Ed.*, 2016, **55**, 4725–4728.

8 V. P. Santos, T. A. Wezendonk, J. J. Delgado Jaén, A. I. Dugulan, M. A. Nasalevich, H. Islam, A. Chojecki, S. Sartipi, X. H. Sun, A. A. Hakeem, A. C. J. Koeken, M. Ruitenbeek, T. Davidian, G. R. Meima, G. Sankar, F. Kapteijn, M. Makkee and J. Gascon, *Nat. Commun.*, 2015, **6**, 6451.

9 G. G. Liu, Q. J. Chen, E. Oyunkhand, S. Y. Ding, N. Yamane, G. H. Yang, Y. Yoneyama and N. Tsubaki, *Carbon*, 2018, **130**, 304–314.

10 J. Z. Lu, L. J. Yang, B. L. Xu, Q. Wu, D. Zhang, S. J. Yuan, Y. Zhai, X. Z. Wang, Y. N. Fan and Z. Hu, *ACS Catal.*, 2014, **4**, 613–621.

11 X. Q. Chen, D. H. Deng, X. L. Pan, Y. F. Hu and X. H. Bao, *Chem. Commun.*, 2015, **51**, 217–220.

12 M. Oschatz, W. S. Lamme, J. X. Xie, A. I. Dugulan and K. P. de Jong, *ChemCatChem*, 2016, **8**, 2846–2852.

13 M. Oschatz, S. Krause, N. A. Krans, C. H. Mejía, S. Kaskelb and K. P. de Jong, *Chem. Commun.*, 2017, **53**, 10204–10207.

14 Y. Cheng, J. Lin, K. Xu, H. Wang, X. Y. Yao, Y. Pei, S. R. Yan, M. H. Qiao and B. N. Zong, *ACS Catal.*, 2016, **6**, 389–399.

15 X. P. Zhou, J. Ji, D. Wang, X. Z. Duan, G. Qian, D. Chen and X. G. Zhou, *Chem. Commun.*, 2015, **51**, 8853–8856.

16 P. Zhai, C. Xu, R. Gao, X. Liu, M. Z. Li, W. Z. Li, X. P. Fu, C. J. Jia, J. L. Xie, M. Zhao, X. P. Wang, Y. W. Li, Q. W. Zhang, X. D. Wen and D. Ma, *Angew. Chem., Int. Ed.*, 2016, **55**, 9902–9907.

17 Z. J. Li, T. J. Lin, F. Yu, Y. L. An, Y. Y. Dai, S. G. Li, L. S. Zhong, H. Wang, P. Gao, Y. H. Sun and M. Y. He, *ACS Catal.*, 2017, **7**, 8023–8032.

18 H. M. Torres Galvis, J. H. Bitter, T. Davidian, M. Ruitenbeek, A. I. Dugulan and K. P. de Jong, *J. Am. Chem. Soc.*, 2012, **134**, 16207–16215.

19 J. X. Xie, H. M. Torres Galvis, A. C. J. Koeken, A. Kirilin, A. I. Dugulan, M. Ruitenbeek and K. P. de Jong, *ACS Catal.*, 2016, **6**, 4017–4024.

20 M. Casavola, J. Hermannsdörfer, N. de Jonge, A. I. Dugulan and K. P. de Jong, *Adv. Funct. Mater.*, 2015, **25**, 5309–5319.

21 E. de Smit and B. M. Weckhuysen, *Chem. Soc. Rev.*, 2008, **37**, 2758–2781.

22 Q. P. Cheng, Y. Tian, S. S. Lyu, N. Zhao, K. Ma, T. Ding, Z. Jiang, L. H. Wang, J. Zhang, L. R. Zheng, F. Gao, L. Dong, N. Tsubaki and X. G. Li, *Nat. Commun.*, 2018, **9**, 3250.

23 B. Yue, Y. W. Ma, H. S. Tao, L. S. Yu, G. Q. Jian, X. Z. Wang, X. S. Wang, Y. N. Lu and Z. Hu, *J. Mater. Chem.*, 2008, **18**, 1747–1750.

24 S. J. Jiang, Y. W. Ma, G. Q. Jian, H. S. Tao, X. Z. Wang, Y. N. Fan, Y. N. Lu and Y. Chen, *Adv. Mater.*, 2009, **21**, 4953–4956.

25 S. Chen, J. Y. Bi, Y. Zhao, L. J. Yang, C. Zhang, Y. W. Ma, Q. Wu, X. Z. Wang and Z. Hu, *Adv. Mater.*, 2012, **24**, 5593–5597.

26 J. Zhao, H. W. Lai, Z. Y. Lyu, Y. F. Jiang, K. Xie, X. Z. Wang, Q. Wu, L. J. Yang, Z. Jin, Y. W. Ma, J. Liu and Z. Hu, *Adv. Mater.*, 2015, **27**, 3541–3545.

27 Z. Y. Lyu, D. Xu, L. J. Yang, R. C. Che, R. Feng, J. Zhao, Y. Li, Q. Wu, X. Z. Wang and Z. Hu, *Nano Energy*, 2015, **12**, 657–665.

28 T. W. Hansen, A. T. Delariva, S. R. Challa and A. K. Datye, *Acc. Chem. Res.*, 2013, **46**, 1720–1730.

29 E. D. Goodman, J. A. Schwalbe and M. Cargnello, *ACS Catal.*, 2017, **7**, 7156–7173.

30 H. Okamoto, *J. Phase Equilib.*, 1992, **13**, 543–565.

31 L. Ratke and P. W. Voorhees, *Growth and Coarsening: Ostwald Ripening in Material Processing*, Springer-Verlag, New York, 2002, pp.117–126.

32 M. Claeys, M. E. Dry, E. van Steen, P. J. van Berge, S. Booyens, R. Crous, P. van Helden, J. Labuschagne, D. J. Moodley and A. M. Saib, *ACS Catal.*, 2015, **5**, 841–852.

33 W. Janse van Rensburg, P. van Helden, D. J. Moodley, M. Claeys, M. A. Petersen and E. van Steen, *J. Phys. Chem. C*, 2017, **121**, 16739–16753.

34 D. Astruc, *Organometallic Chemistry and Catalysis*, Springer-Verlag, Berlin, 2007, pp. 152–153.

35 J. Van Wonterghem, S. Mørup, S. W. Charles, S. Wells and J. Villadsen, *Phys. Rev. Lett.*, 1985, **55**, 410–413.

36 E. de Smit, F. Cinquini, A. M. Beale, O. V. Safonova, W. van Beek, P. Sautet and B. W. Weckhuysen, *J. Am. Chem. Soc.*, 2010, **132**, 14928–14941.

37 P. Atkins and J. de Paula, *Physical Chemistry: Thermodynamics, Structure, and Change*, Oxford Univ. Press, 2014, vol. 689, pp. 254–256.

38 R. E. Winters and R. W. Kiser, *Inorg. Chem.*, 1964, **3**, 699–702.
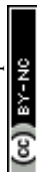
39 J. P. Xiao, X. L. Pan, S. J. Guo, P. J. Ren and X. H. Bao, *J. Am. Chem. Soc.*, 2015, **137**, 477–482.

40 B. Zhao, P. Zhai, P. F. Wang, J. Q. Li, T. Li, M. Peng, M. Zhao, G. Hu, Y. Yang, Y. W. Li, Q. W. Zhang, W. B. Fan and D. Ma, *Chem*, 2017, **3**, 323–333.

41 P. Munnik, M. E. Z. Velthoen, P. E. de Jongh, K. P. de Jong and C. J. Gommes, *Angew. Chem., Int. Ed.*, 2014, **53**, 9493–9497.

42 W. T. Ralston, G. Melaet, T. Saephan and G. A. Somorjai, *Angew. Chem., Int. Ed.*, 2017, **56**, 7415–7419.

43 C. Yang, H. B. Zhao, Y. L. Hou and D. Ma, *J. Am. Chem. Soc.*, 2012, **134**, 15814–15821.